Geoderma 293 (2017) 44–53

Contents lists available at ScienceDirect

Geoderma

journal homepage: www.elsevier.com/locate/geoderma

Microscale soil structures foster organic matter stabilization in permafrost soils

Carsten W. Mueller [a,*], Carmen Hoeschen [a], Markus Steffens [a], Henning Buddenbaum [b], Kenneth Hinkel [c], James G. Bockheim [d], Jenny Kao-Kniffin [e]

[a] Lehrstuhl für Bodenkunde, TU München, Freising-Weihenstephan 85356, Germany
[b] Environmental Remote Sensing and Geoinformatics, University of Trier, 54286 Trier, Germany
[c] University of Cincinnati, Department of Geography, Cincinnati, OH 45221, USA
[d] Department of Soil Science, University of Wisconsin-Madison, Madison, WI 53706, USA
[e] Department of Horticulture, Cornell University, Ithaca, NY 14853, USA

ARTICLE INFO

Article history:
Received 24 October 2016
Accepted 24 January 2017
Available online xxxx

Keywords:
Particulate organic matter
Mineral associated organic matter
Micro aggregate
NanoSIMS
SEM
Supervised image classification

ABSTRACT

Organic carbon (OC) stored in permafrost affected soils of the higher northern latitudes is known to be highly vulnerable to ongoing climatic change. Although the ways to quantify soil OC and to study connected C dynamics from ecosystem to global scale in the Arctic has improved substantially over the last years, the basic mechanisms of OC sequestration are still not well understood. Here we demonstrate a first approach to directly study micro scale soil structures mainly responsible for soil OC (SOC) stabilization using nano scale secondary ion mass spectrometry (NanoSIMS). A cross section from a permafrost layer of a Cryosol from Northern Alaska was analysed using a cascade of imaging techniques from reflectance light microscopy (RLM) to scanning electron microscopy (SEM) to NanoSIMS. This allowed for the direct evaluation of micro scale soil structures known to be hot spots for microbial activity and SOC stabilization in temperate soils. The imaging techniques were supported by classical soil analyses. Using this unique set of techniques we are able to evidence the formation of micro-aggregate structures in the vicinity of plant residues in permafrost soils. This clearly indicates biogeochemical interfaces at plant surfaces as important spheres for the formation of more complex soil structures in permafrost soils. Organo-mineral associations from these hot spots of microbial activity were recovered from plant residues (free particulate organic matter, fPOM) as fine grained mineral fraction with a typically low C/N ratio. This nicely illustrates the link between classical bulk analysis and state of the art spectromicroscopic techniques.

1. Introduction

More than twice as much organic carbon (OC) than in the atmosphere is estimated to be stored in permafrost affected soils of the northern hemisphere (Hugelius et al., 2014). Predicted changes in the arctic carbon cycling solely consider the active layer thawing during summer while assuming it as a homogeneous carbon reservoir (Schuur et al., 2008). This is in clear contrast to the known heterogeneity of the composition and spatial distribution of soil OC (SOC) and thus possible future changes in microbial bioavailability (Gentsch et al., 2015; Höfle et al., 2013; Knoblauch et al., 2013; Mueller et al., 2015; Schädel et al., 2014; Vonk and Gustafsson, 2013). It is still not fully understood which mechanisms might replace the climatic stabilization of SOC (reduced mineralization due to low temperatures) (Trumbore, 2009) and thus possibly sustain long term SOC storage in the future with pronounced warming in polar regions. Due to the fact that active layers will deepen and large amounts of buried mostly labile OC (Gillespie et al., 2014; Mueller et al., 2015; Palmtag et al., 2016) might be exposed to more favorable conditions in terms of SOC mineralization. From temperate soils it is known that soil structure plays a vital role for the long term sequestration of OC by the occlusion of particulate organic matter (POM) within aggregates and the association of OC with mineral micro-aggregate structures (Vogel et al., 2014; von Lützow et al., 2008). Although permafrost affected soils are characterized by drastic freeze–thaw cycles leading to the vertical mixing of different soil compartments (cryoturbation), there is growing evidence that soil structural features (e.g. micro-aggregates) also affect SOC sequestration in permafrost affected soils. For instance for soils in northern Alaska and Siberia a substantial amount of particulate SOC was found to be sequestered occluded within aggregated soil structures (Höfle et al., 2013; Mueller et al., 2015). Recent incubation experiments highlighted the contribution and importance of organo-mineral associations for SOC sequestration in soils of the Siberian Arctic, with over 50% of soil OC bound to minerals (Gentsch et al., 2015).

* Corresponding author.
E-mail address: carsten.mueller@wzw.tum.de (C.W. Mueller).

http://dx.doi.org/10.1016/j.geoderma.2017.01.028
0016-7061/

However, these findings are based on bulk analyses which are defined by the destruction of the intact soil structure and thus integrate over a larger volume. To directly study soil structure and elemental distribution together, it is crucial to keep the soil microscale architecture intact (Mueller et al., 2013). The systematic study of intact in-situ soil structures dates back to the micropedological work of Kubiena (1938). Intact soil samples were resin embedded and polished, and pedological features were studied on the resulting thin sections using transmitted light microscopy. Over the years this technique was used to study a wide variety of soils including permafrost affected soils (Bullock and Murphy, 1980; Eickhorst and Tippkoetter, 2008; Fisk et al., 1999; Li et al., 2004; Murton et al., 2015; Pulleman et al., 2005; Smith et al., 1991; Szymanski et al., 2015). But the micromorphological approach is often restricted to the description of structural features due to the limited capabilities of visible light microscopic techniques. With the advent of microscopic techniques resolving soil features together with elemental and molecular information at the nano- to micro-scale (e.g. scanning electron microscopy (SEM), time of flight secondary ion mass spectrometry (TOF-SIMS), nano scale secondary ion mass spectrometry (NanoSIMS)), the micromorphological examination of soils may change from the pure description of soil structures to the identification of materials and analyses of soil processes. Thus, the increased accessibility of spectromicroscopic techniques allows nowadays for the evaluation of micro-scale structural entities and biogeochemical features and processes which determine the long term stabilization of SOC. In the present study we combine the classical micromorphological approach of soil embedding and sectioning with state of the art NanoSIMS to elucidate elemental distributions at soil microenvironments. To account for the spatial representation of the spots analysed at high resolution by NanoSIMS, we used conventional reflectance light microscopy together with supervised image classification. This allowed for the identification of structural domains representing specific biogeochemical interfaces and thus areas which may act as hot spots for SOC stabilization, microbial activity, nutrient sorption and cycling.

2. Materials and methods

2.1. Sampling site and soil material

Samples were taken at the Barrow Peninsula, on the Arctic Coastal Plain in April 2010. For a more detailed description of the sampling campaign see Mueller et al. (2015). The landscape is characterized by a mosaic of drained thaw lake basins with a different age since drainage. For the study we took samples from a soil core (at 71.27786 latitude and 156.44264 longitude) of an Aquiturbel (Soil Survey Staff, 2010), see Table 1 for basic soil properties. The core originated from a drained thaw lake basin of medium age (approx. 50 to 300 years after thaw lake drainage) according to the classification given by Hinkel et al. (2003). The parent material consists of unconsolidated sediments of the Late Pleistocene Gubik Formation (Hinkel et al., 2003). The soil core was obtained using a SIPRE corer attached to a Big Beaver earth drill apparatus (Little Beaver, Inc., Livingstone, TX) mounted on a sledge. The frozen core was further processed in a cold room in Barrow and after horizon description cut into sections of corresponding soil horizons. Samples for general soil properties were dried at 60 °C in an oven in Barrow and subsequently shipped to Germany.

Table 1
Soil properties of the analysed Cryosol core. The embedded soil section was taken from the deepest horizon (Cg/Oabfm).

Horizon	Depth [cm]	Bulk density [g*cm^{-3}]	OC [mg*g^{-1}]	N [mg*g^{-1}]	C/N
Oi1	0–12	0.13	413.5	19.7	21.0
Oi2	12–14	0.27	324.8	14.3	22.7
Cg/Oijj	14–40	0.66	103.5	6.2	16.7
Cg/Oejjfm	40–80	0.60	97.9	6.5	15.0
Cg/Oabfm	80–126	0.67	30.3	1.9	16.4

2.2. Intact sample preparation and NanoSIMS

Subsections of the intact frozen cores were initially dried with acetone (row of different concentration) and then impregnated with a series of Araldite 502:acetone mixtures (1:3, 1:1 (vl:vl)) and finally with 100% Araldite 502 (Araldite kit 502, electron microscope sciences, Hatfield, USA). The blocks (24.5 mm in diameter) were cured at 60 °C for 48 h, cut into thin slices and carefully polished. Due to the insulating properties of the epoxy resin, the epoxy blocks were gold-coated by physical vapour deposition under argon atmosphere prior to SEM and NanoSIMS analysis. Prior to NanoSIMS analysis, the samples were investigated using a reflectance light microscope (further denominated as: RLM; Zeiss Axio Imager Z2) and a scanning electron microscope (SEM; Jeol JSM 5900LV, Freising, Germany) in backscatter electron mode. Due to the flat polishing of the section the material contrast of the backscattered electrons allowed for a good differentiation between organic and mineral compartments while also allowing the identification of soil pores filled with the epoxy resin.

The NanoSIMS images were recorded at the Cameca NanoSIMS 50 L (Gennevilliers, France) of the Lehrstuhl für Bodenkunde, TU München, Germany.

Electron multiplier secondary ion collectors were used for $^{12}C^-$, $^{16}O^-$, $^{12}C^{14}N^-$, $^{28}Si^-$, $^{32}S^-$, $^{27}Al^{16}O^-$ and $^{56}Fe^{16}O^-$. Charging was compensated by an electron beam generated by the electron flood gun of the NanoSIMS instrument. Prior to analysis, impurities and the coating layer were sputtered away by using a high primary beam current.

2.3. Physical soil fractionation

To relate the image data with the distribution of main soil constituents we conducted a combined density and particle size fractionation procedure according to Mueller et al. (2015). Air dried soil material (20 g) was capillary-saturated with sodium polytungstate solution (1.8 g cm^{-3}) and allowed to settle overnight. The floating free particulate organic matter (fPOM) was extracted prior to ultrasonic disruption (Bandelin, Sonopuls HD 2200; energy input of 440 J ml^{-1}) of aggregated soil structures and the recovery of occluded POM (oPOM). Excess salt from POM fractions was removed by washing with deionised water over a sieve of 20 μm mesh size until the electric conductivity dropped below 5 μS cm^{-1}. The procedure yielded two large POM fractions (fPOM, oPOM) and two smaller POM fractions <20 μm (fPOM$_{small}$ and oPOM$_{small}$). Mineral fractions larger than 20 μm were separated by wet sieving, all smaller mineral fractions were obtained by sedimentation. All fractions were freeze-dried, weighed and analysed for C and N content.

2.4. Chemical analyses

For bulk chemical analysis the soil material was ground using a ball mill (Fritsch, Germany, pulverisette 23). Carbon and nitrogen contents were measured in duplicate by dry combustion (EuroVector, Milan, Italy). Due to the absence of carbonates, the measured C concentrations equalled organic C.

2.5. Statistical analyses and image processing

To evaluate the spatial extent of the areas analysed using NanoSIMS, we conducted a supervised maximum likelihood classification (MaxLike) on the RLM image in the image processing software Envi (Version 5.2, ITT Visual Information Solutions). The MaxLike algorithm assumes that the statistics for each class in each band are normally distributed and calculates the probability that a given pixel belongs to a

specific class. No probability threshold was used and all pixels were assigned to the class that has the highest probability based on the following discriminant functions (Richards and Jia, 1999):

$$g_i(\boldsymbol{x}) = \ln p(\omega_i) - \frac{1}{2}\ln|\Sigma_i| - \frac{1}{2}(\boldsymbol{x}-\boldsymbol{m}_i)^t \Sigma_i^{-1}(\boldsymbol{x}-\boldsymbol{m}_i) \quad (1)$$

where$i$ = class$\boldsymbol{x}$ = n-dimensional data (where n is the number of bands)$p(\omega_i)$ = probability that class ω_i occurs in the image and is assumed the same for all classes$|\Sigma_i|$ = determinant of the covariance matrix of the data in class wiΣ_i^{-1} = its inverse matrix$\boldsymbol{m}_i$ = mean vector

We visually identified 6 information classes (fresh plant residues, decomposed plant residues, highly decomposed OM, Fe oxides, coarse/medium mineral particles and fine mineral particles) in the RLM image. We selected 89 training areas (3 to 50 areas per class) to define the reference spectra for each class and used a fixed set of reference spectra for the classification.

3. Results

3.1. Fresh and altered particulate organic matter

The soil material contained considerable amounts of plant residues (particulate organic matter, POM) at different stages of decomposition. These plant residues, accounting for 58% of the OC stored in the analysed soil (Table 2), could be recovered by physical fractionation (Table 2) and visualized using reflectance light microscopy (Fig. 1), scanning electron microscopy (SEM; Fig. 2) and nano-scale secondary ion mass spectrometry (NanoSIMS; Figs. 3 to 6). Using soil physical fractionation yielding quantitative information about the mass distribution and C and N content of free and occluded OM, clearly pointed to the high importance of free particulate OM (fPOM) for SOC storage (Table 2) in the permafrost layer. Besides rather fresh SOM with a sharp boundary to the mineral soil matrix, imaging revealed more complex aggregated structures with associations between mineral and organic particles forming extensive organo-mineral soil structures. The occluded POM (Table 2) recovered by physical soil fractionation represents SOC stored in such soil aggregates. The backscattered electron micrograph of the area indicated as A in the reflectance light micrograph in Fig. 1, is displayed in Fig. 2 A, demonstrating the sharp delimitation between the silt to medium sand textured soil matrix and the organic particles. Two main SOM constituents representing POM end members were recorded, namely the fresh POM of a plant stem (Fig. 2A, ps) and the amorphous OM of highly altered POM (Fig. 2A, aOM). The microscale distribution of the OM at these areas was visualized as $^{12}C^{14}N^-$ detected by NanoSIMS (Fig. 3). The distribution of the $^{12}C^{14}N^-$ of the fresh plant material showed the unaltered OM distribution reflecting the intact cell structures with no distinct differences in terms of ion counts (Fig. 3A). The patch with rather high counts of secondary ions in the central plant cell represents residues from the polishing processes remaining in a hollow formed by an air bubble of the embedding resin. Unaltered fresh plant residues are highlighted in green in the RLM classification results (Fig. 7) with a total area of 1.9% of the cross section. In contrast to the unaltered plant tissue, Fig. 3(B) shows collapsed plant cells of POM that appears as dark spots in the reflectance light microscope (Fig. 1A) or as amorphous matter in the SEM image (Fig. 2A 2), highlighted in blue in the RLM classification (Fig. 7, Table 3) with a total area of 41.1% of the analysed sample. The $^{12}C^{14}N^-$ distribution shows clear differences in the secondary ion counts with clear maxima at some spots. In contrast to the consistent dark appearance in the reflected light, the $^{12}C^{14}N^-$ distribution clearly indicates a sponge-like structure of this amorphous OM with a lot of pores which are filled with epoxy resin, appearing here as blue background in the $^{12}C^{14}N^-$ image.

A third form of plant residues is shown in Fig. 2B representing the cross section of the intact structures of a moss plant (Fig. 1B). The backscattered SEM image clearly demonstrates the high amount of fine textured mainly silt sized mineral particles entrapped within the leaf-like structures, whereas around the plant structures the texture is dominated by medium sized sand, a matrix that dominates the sample as demonstrated by the high amount of fine sand and coarse silt and classified as fine mineral matrix in the RLM image (Table 2, Fig. 7). The plant structure as a whole also showed a clear delimitation towards the sandy soil matrix. In Fig. 4A the composite image of the distribution of the secondary ions $^{12}C^{14}N^-$, $^{56}Fe^{16}O^-$ and $^{27}Al^{16}O^-$ are displayed, indicating the formation of interfaces between OM and mineral soil constituents. In Fig. 4B a lateral profile is given, indicated as white arrow in Fig. 4A, of the three secondary ion species normalized for $^{16}O^-$. Following the lateral profile the plant residues are clearly depicted by the peaks in $^{12}C^{14}N^-$ at 0 to 10 μm and 20 to 25 μm of the line scan distance. The distribution of the $^{27}Al^{16}O^-$ secondary ions is demonstrating a matrix dominated by clay minerals, whereas pedogenic iron oxides are indicated by small patches of $^{56}Fe^{16}O^-$. Such a small iron sphere is indicated by the $^{56}Fe^{16}O^-$ peak at 15.6 μm of the line scan distance in Fig. 4C directly following the $^{27}Al^{16}O^-$ peak indicating the interface

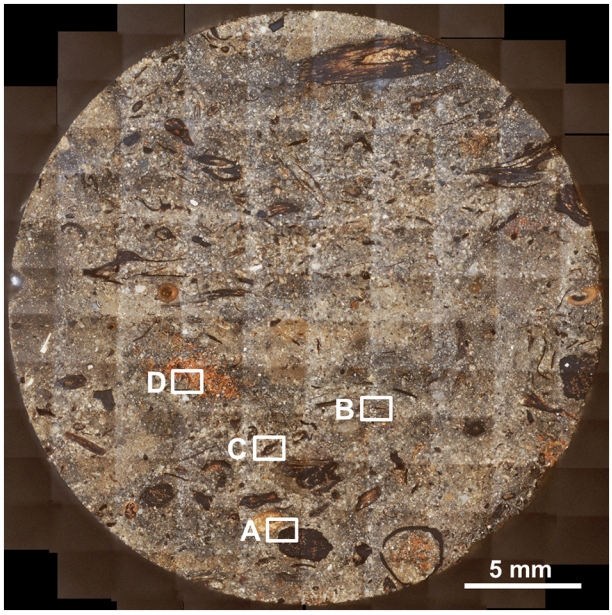

Fig. 1. Reflectance light microscopic image of the embedded, polished Cryosol section. The sample originates from the Cg/Oabfm horizon (~110 cm depth) of an Aquiturbel near Barrow, Alaska. The white squares indicate regions analysed in more detail using scanning electron microscopy and nano-scale secondary ion mass spectrometry.

Table 2
Content, organic carbon and nitrogen contents, distribution of OC and C to N ratios of the soil organic matter fractions obtained by density (POM) and particle size fractionation (sand, silt and clay) of the Cg/Oabfm horizon.

Fractions		Content [mg ∗ g^{-1}]	OC	N_{tot}	OC distribution	CN
POM	fPOM	39.5	424.1	10.5	234.2	40.3
	fPOM <20 μm	34.4	179.9	11.1	86.6	16.2
	oPOM	3.3	443.8	13.4	20.2	33.0
	oPOM <20 μm	6.6	300.2	13.5	27.5	22.3
Sand	200 to 2000 μm	35.1	n.d.	n.d.	b.d.l.	n.d.
	63 to 200 μm	432.2	24.5	1.1	147.7	22.3
Silt	20 to 63 μm	218.8	42.1	1.8	128.8	23.7
	6.3 to 20 μm	90.5	103.6	5.4	131.1	19.1
	2 to 6.3 μm	39.3	130.4	7.2	71.7	18.1
Clay	<2 μm	100.3	108.5	7.6	152.2	14.4

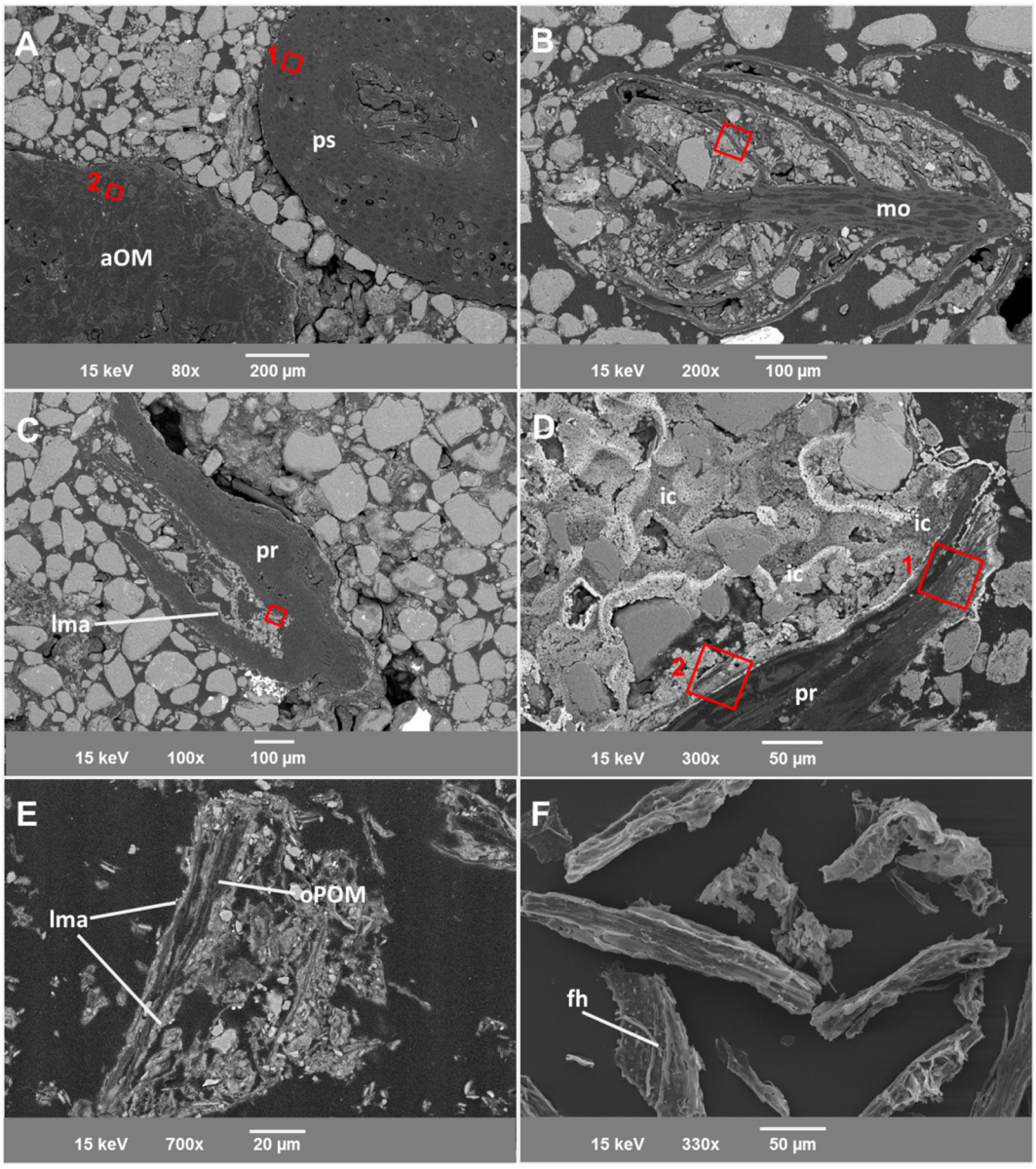

Fig. 2. Scanning electron microscopy (backscattered electron mode) images of the areas indicated in Fig. 1. A) plant stem (ps) and amorphous soil organic matter (aOM), B) moss plant cross section (mo), C) altered plant residues (pr) with associated laminar micro aggregate spheres (lma) and D) quartz grains and organic particle coated with iron oxide coating (ic). In E) a sectioned micro-aggregate derived from bulk soil is displayed with occluded POM (oPOM) and associated mineral particles. Free POM derived from density fractionation is displayed (secondary electron mode) in F) with attached fungal hyphae (fh) on one particle. The red squares in A to D indicate the areas analysed by NanoSIMS. (For interpretation of the references to colour in this figure legend, the reader is referred to the web version of this article.)

between clay minerals and an iron oxide agglomeration. In Fig. 4D the alteration between the single three secondary ion species indicate the close vicinity of different interfaces between the three main constituents, clay, iron oxides and organic matter.

3.2. Biogeochemical interfaces between minerals and particulate organic matter

It was shown that complex biogeochemical interfaces formed at surfaces of particulate organic matter. This was indicated as distinct co-localizations between organic and mineral soil constituents, namely plant residues, clay minerals and iron oxides. The area containing rather altered OM indicated as square C in Fig. 1 is shown as backscattered SEM image in Fig. 2C. The OM particle (plant residue, pr in Fig. 2C) represents a more altered OM with attached fine textured minerals which are in contrast to the coarser texture of the surrounding soil matrix. In Fig. 5A the distribution of the $^{12}C^{14}N^-$ secondary ions illustrates collapsed plant cells comparable to the ones shown in Fig. 3B for altered amorphous OM. The direct interfaces between OM and minerals are demonstrated in the lateral profiles given in Fig. 5B to E, with clear undulating peaks of $^{12}C^{14}N^-$, $^{56}Fe^{16}O^-$ and $^{27}Al^{16}O^-$. The small cell wall residue at 11 µm (Fig. 5B) is covered at both sides by a thin layer of clay minerals (Fig. 5C). The two peaks of $^{56}Fe^{16}O^-$ at 2.5 µm and 7.5 µm (Fig. 5D) indicate the iron oxide coating of quartz grains which are visible as black areas surrounded by the $^{56}Fe^{16}O^-$ given in red in Fig. 5A.

In Fig. 6 data on the elemental distribution of $^{12}C^{14}N^-$, $^{32}S^-$ and $^{56}Fe^{16}O^-$ is given. The analysed areas (Fig. 6A and B) represent a POM particle (plant residue, pr in Fig. 2C) entrapped in a larger area dominated by layered iron oxide deposits co-localized with sulphur (Figs. 1D, 6A

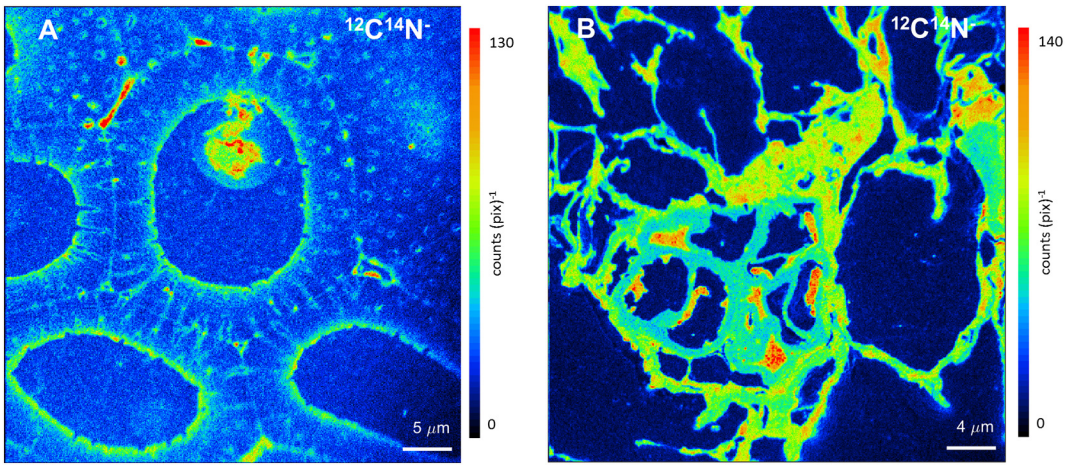

Fig. 3. NanoSIMS images A) $^{12}C^{14}N^-$ image of the area indicated in Fig. 2A 1, B) $^{12}C^{14}N^-$ image of the area indicated in Fig. 2A 2.

and B). The original plant structure is almost absent and also the interior of the plant structure was encrusted with iron oxides as indicated by the red $^{56}Fe^{16}O^-$ distribution within the green OM structures ($^{12}C^{14}N^-$) in Fig. 6.

Fig. 6C and D represent the ratio between $^{56}Fe^{16}O^-$ and $^{32}S^-$, displayed as HSI (hue, saturation, intensity) image.

3.3. Contribution of soil materials and structures evaluated by physical fractionation and light microscopy

Reflectance light microscopy (Fig. 1) was used to evaluate the spatial extent of the areas analysed in more detail using NanoSIMS. A supervised classification based on the visible soil structures was used

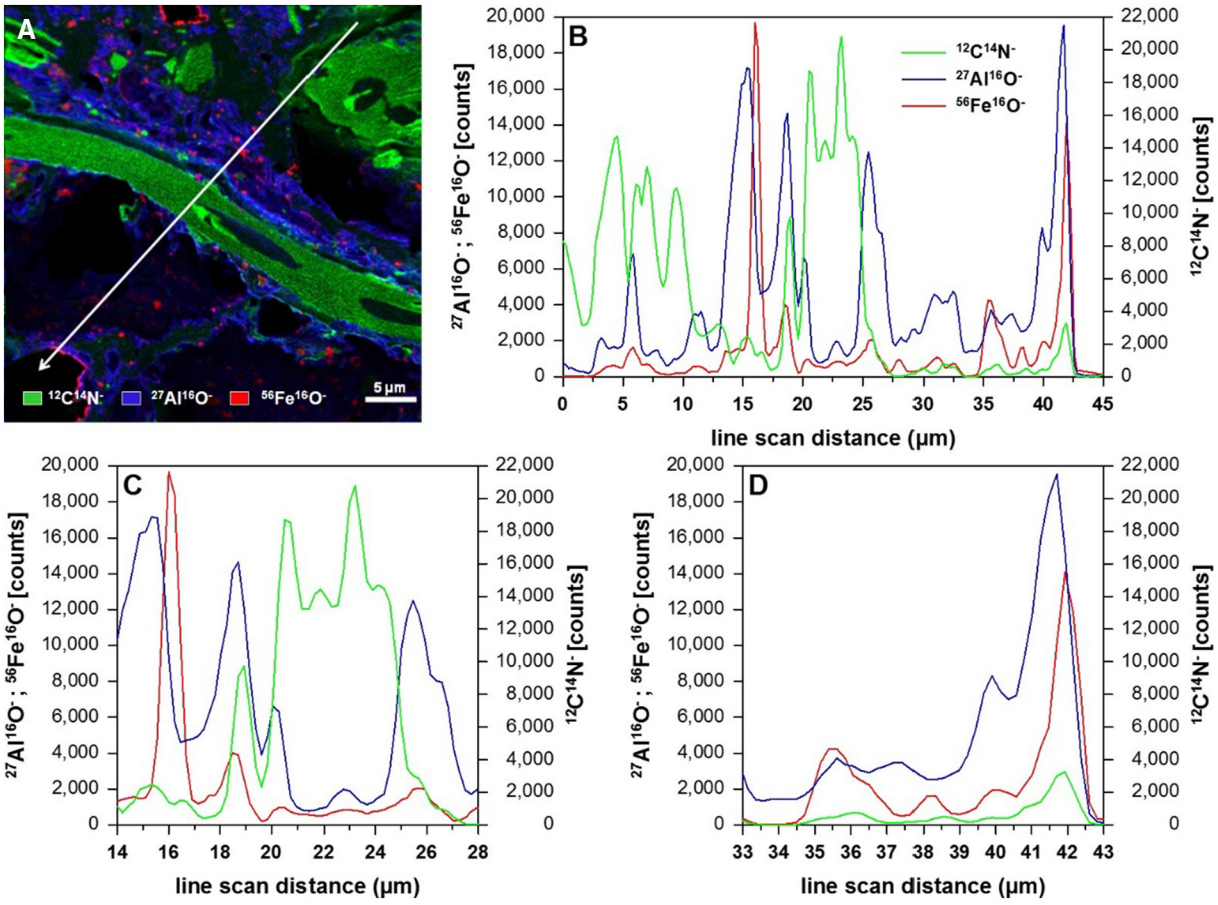

Fig. 4. A) overlay of NanoSIMS images ($^{12}C^{14}N^-$, $^{56}Fe^{16}O^-$ and $^{27}Al^{16}O^-$) of area (red square) indicated in Fig. 2B with white arrow indicating a line scan. The image indicates the distribution of organic matter ($^{12}C^{14}N^-$), clay minerals ($^{27}Al^{16}O^-$) and the iron distribution ($^{56}Fe^{16}O^-$) within the plant cell region, and suggests organo-mineral interfaces in the early stages of formation. B) Secondary ions along the line scan. C) and D) magnified subsections of the line scan data in B. (For interpretation of the references to colour in this figure legend, the reader is referred to the web version of this article.)

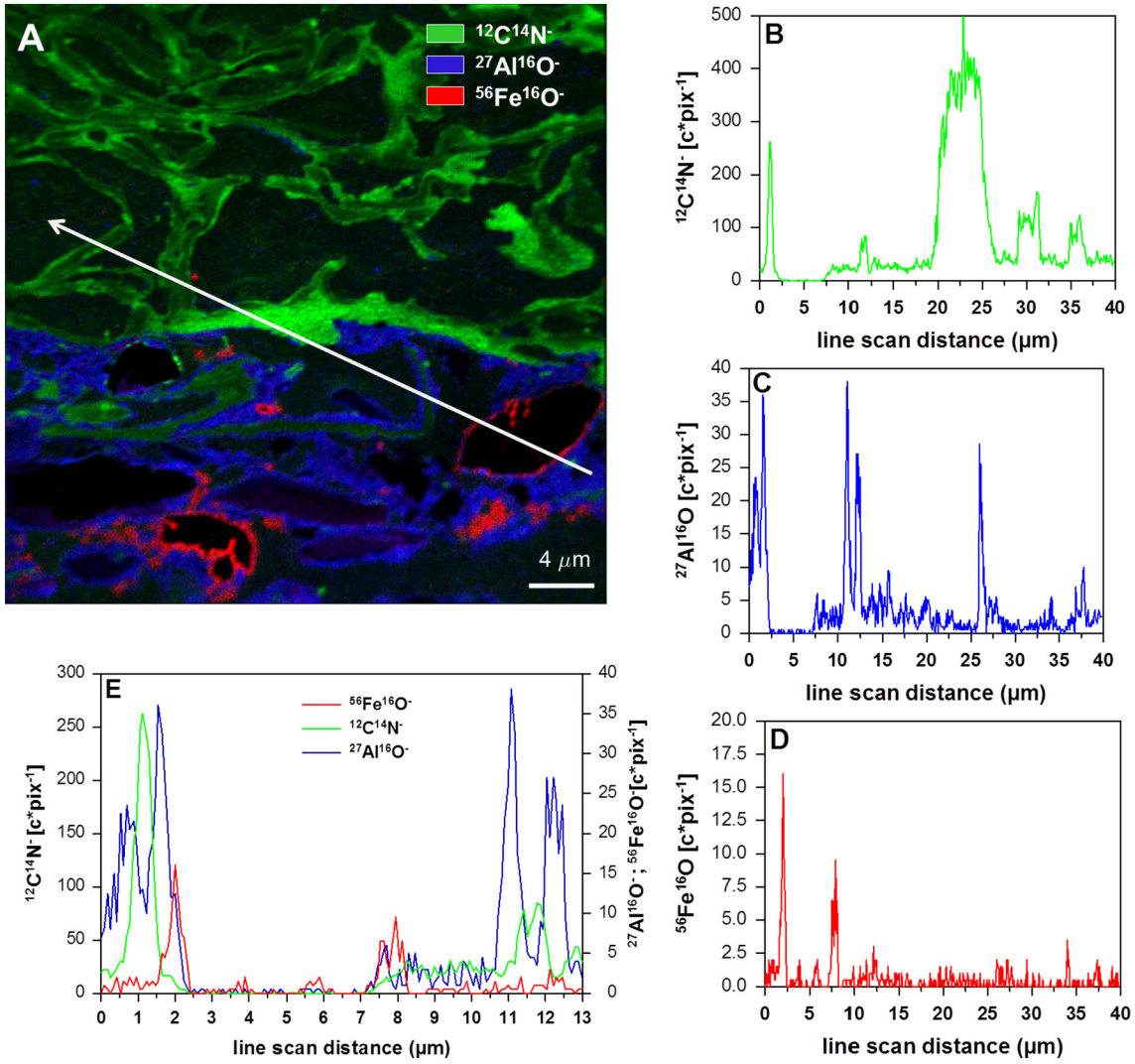

Fig. 5. A) overlay of the NanoSIMS images ($^{12}C^{14}N^-$, $^{56}Fe^{16}O^-$ and $^{27}Al^{16}O^-$) of the section (red square) indicated in Fig. 2C with white arrow indicating a line scan. The image indicate the distribution of organic matter ($^{12}C^{14}N^-$), clay minerals ($^{27}Al^{16}O^-$) and the iron distribution ($^{56}Fe^{16}O^-$) within the plant cell region, and shows organo-mineral interfaces in the early stages of formation. B), C), D) and E) $^{12}C^{14}N^-$, $^{27}Al^{16}O^-$ and $^{56}Fe^{16}O^-$ secondary ions normalized for $^{16}O^-$ along the line scan shown in A. (For interpretation of the references to colour in this figure legend, the reader is referred to the web version of this article.)

(Figs.s 1 and 7, Table 3), aiming to correlate physical SOM fractions (Table 2) with the visualization results. The classification result in Fig. 7 indicated a very good separation of distinct soil structures based on reflectance light microscopy partly matching SOM fractions. The supervised classification (Fig. 7) links partly to the obtained SOM fractions, with the plant residues indicative for the POM fractions and the mineral matrix and iron oxides indicative for the mineral soil fractions. Due to the different approaches, supervised image classification versus physical soil fractionation, the distinct soil features were not named according to SOM fractions but visible soil features. As it is not possible to differentiate between occluded and free POM, the degree of decomposition according to colour was used, with a dominance of decomposed plant residues (Table 3). The 'fresh plant residues' can be attributed to fPOM, whereas it can be assumed that more altered plant residues (decomposed plant residues and highly decomposed OM) attribute both to fPOM and oPOM fractions. The Fe oxides and fine mineral particles can mostly be attributed to the fine mineral fractions (clay, silt and partly fine sand), whereas the coarse mineral particles in Fig. 7 represent mostly the sand fraction. A clearly higher contribution of mineral than organic materials was classified (Fig. 7 and Table 3), with 43.1% organic and 56.9% mineral materials, respectively. This corresponds to the results of the physical fractionation given in Table 2, showing a clear dominance of fine sand and coarse silt. These mineral materials were classified as fine mineral matrix shown in Fig. 7. At the same time the image classification also clearly revealed the high amount of particulate SOM, which accounts for 58% of the stored OC in the analysed soil.

4. Discussion

4.1. Microscale features – from plant residues to organic matter interfaces

Free particulate organic matter in the studied soil section occurs as either fresh mostly undecomposed plant residues (Fig. 2A; plant stem) or as highly altered plant derived OM (Fig. 2A; aOM). The high amount of particulate OM not associated with soil minerals is supported by the high amount of recovered fPOM in the buried O horizon material (Table 2). This is also supported by the high amount of plant residues classified in the section shown in Fig. 7. As demonstrated by Mueller et al. (2015) for soils from the same sampling campaign, the fPOM was mostly dominated by less decomposed OM demonstrated by high amounts of O/N alkyl C and constituted the major OC pool especially in older soils. The low degree of decomposition is also demonstrated by intact cell structures dominating the fPOM recovered by density

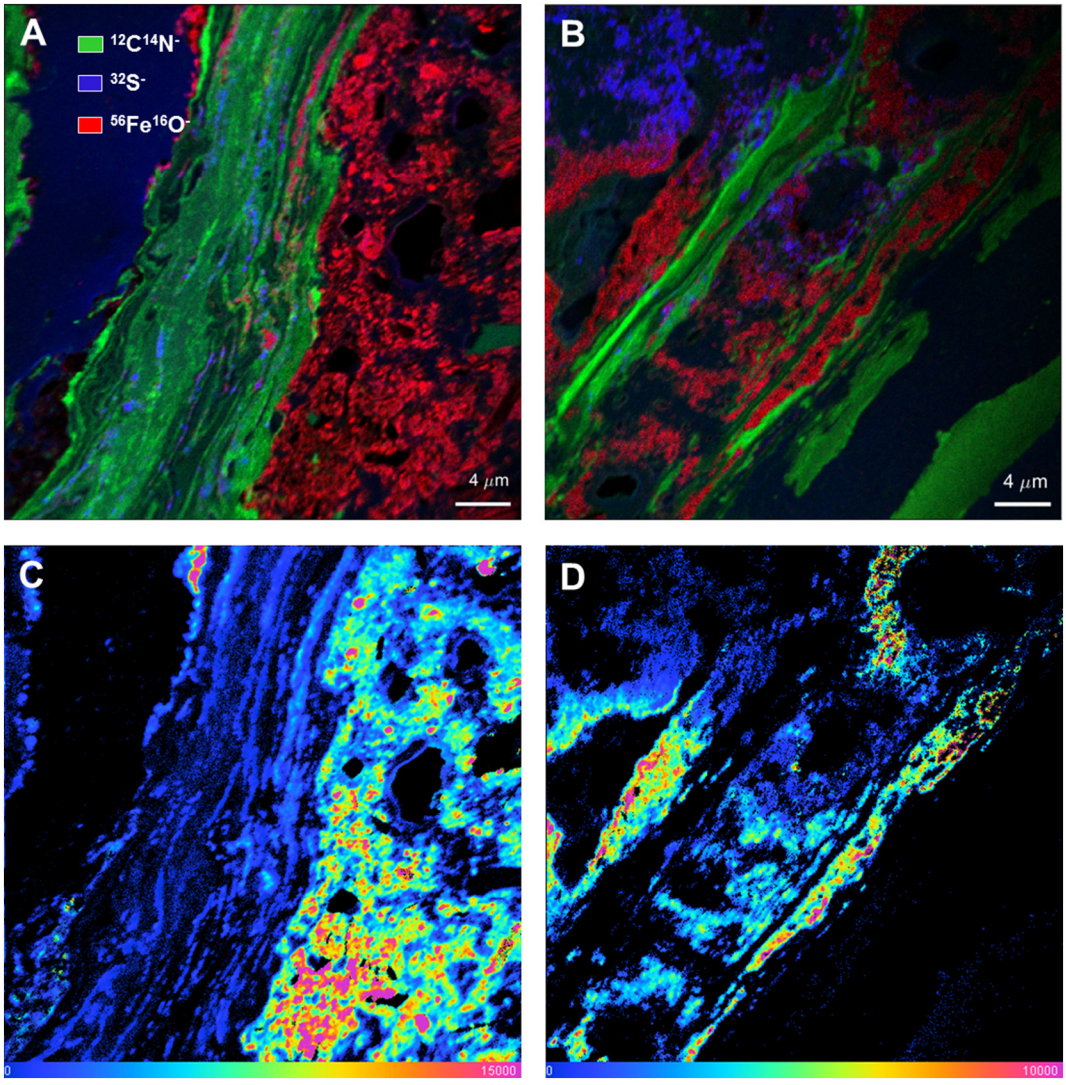

Fig. 6. A) and B) Overlay of NanoSIMS images ($^{12}C^{14}N^-$, $^{32}S^-$ and $^{56}Fe^{16}O^-$) of the area (red squares) indicated in Fig. 2D, 1 (A) and 2 (B). The images indicate the distribution of organic matter ($^{12}C^{14}N^-$), iron oxides ($^{56}Fe^{16}O^-$) and sulphur (the $^{32}S^-$). C) and D) HSI (hue, saturation, intensity) image of the $^{56}Fe^{16}O^-/^{32}S^-$ ratios. (For interpretation of the references to colour in this figure legend, the reader is referred to the web version of this article.)

fractionation (Fig. 2F), whereas the attached fungal hyphae (Fig. 2F, fh) clearly indicate the high potential microbial activity at plant surfaces. The results of the MaxLike classification (Fig. 7 and Table 3) point to a darker appearance of the POM in the permafrost layer.

Whereas Fig. 3 A shows the distribution of OM ($^{12}C^{14}N^-$) in conserved unaltered plant cells, Fig. 3 B shows the collapsed cell structures of highly altered plant residues, a material which was classified as highly decomposed OM in the RLM image representing 23.5% of the thin section area. In the $^{12}C^{14}N^-$ measurement of Fig. 3 B a more even distribution of the secondary ions than in the unaltered plant structure clearly indicate the increased amount of microbial derived OM during decomposition. This is supported by findings of Hatton et al. (2015) who assumed increased microbial derived N at micro-scale spots indicated by narrow C/N ratios calculated based on NanoSIMS measurements of density fractions. In contrast to the mineral-associated OM from disrupted soils analysed by Hatton et al. (2015), we can show the enrichment in N for fragmented decomposed plant material in an intact soil structure. Such small scale distribution of N, presumably especially dominated by microbial derived N, cannot be evaluated by classical bulk analysis. Also the differentiation into physical soil fractions widely used to analyse specific soil constituents and SOC pools, is not sufficient to recover such micro scale spheres. Although there are considerable differences of the C/N ratios between different POM fractions, except the $fPOM_{small}$ which is mostly mineral-associated OM, such ratios only demonstrate a mean over a wide variety of differently altered OM particles. It might be assumed that the N rich OM particles may serve as hot spot for microbial activity when the active layer gets deeper, and OM now stabilized in the permafrost will get unfrozen. Gentsch et al. (2015), who studied the bioavailability of light and heavy SOM fractions in laboratory incubations of Cryosols from Siberia, were able to demonstrate the high vulnerability of SOC for mineralization in light particulate SOM to favorable environmental conditions (e.g. increased temperatures).

4.2. Increased complexity at interfaces between mineral and organic particles

Besides OM particles located freely within the fine sand dominated soil structure (Figs. 2A and 3), there also exists a considerable number of more complex plant residues which can be assumed as important agents for soil structure formation. Such structures are shown in Fig. 2B, C and D. These images evidence the early stages of the formation of aggregated soil structures in permanently frozen horizons. This aggregation is demonstrated by the embedded intact bulk soil cross section (disturbed bulk soil material from the same horizon was used for fractionation) shown in Fig. 2E, with clearly visible occluded POM and

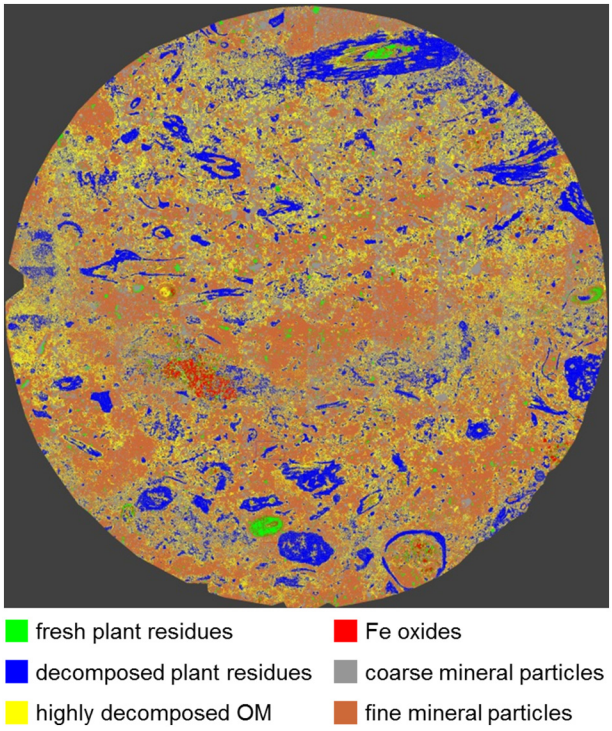

Fig. 7. Supervised maximum likelihood classifications of the whole cross section disk of the embedded Cryosol for the real colour image (RGB) taken with a reflectance light microscope (RLM). (For interpretation of the references to colour in this figure legend, the reader is referred to the web version of this article.)

the associated laminar micro aggregate like structures (lma) at the surface of the plant residues. Here the intact plant residue act as a 'priming structure' for the aggregation of fine grained mineral particles in a mineral soil matrix dominated by coarse silt and fine sand. Especially in Fig. 2B it is visible how fine mineral material of silt and clay size (<~63 μm) is entrapped in the intact plant structures surrounded by the sandy bulk soil matrix. Such plant structures were recovered as occluded particulate OM (oPOM) by density separation. For occluded POM fractions from the same sampling campaign lower ^{14}C contents compared to free POM were reported by Mueller et al. (2015). This suggests a reduced bioavailability of this occluded OC pool where physical accessibility for microbes is restricted. Thus, comparable to what was shown for temperate soils (von Lützow et al., 2008), these oPOM particles represent an OC pool which is sequestered on a longer term. But these particles seem to have also an important function as nuclei for soil aggregation and thus the formation of new biogeochemical interfaces between fine mineral particles and plant residues (Totsche et al., 2010). In Fig. 5B such a hot spot is shown as a plant cell residue which is at both sides covered by a thin layer of clay minerals (Fig. 5C). A comparable aggregation at a comparable organic hot spot for soil structure formation was reported by Dormaar and Foster (1991) for the rhizosphere of ryegrass. Such organic surfaces, either living rhizospheres or decaying plant residues, represent zones of high microbial activity and thus also areas with a high amount of microbial residues. These organic surfaces are known to play a key role in the development and stability of soil aggregates (Martens, 2000; Oades and Waters, 1991; Tisdall and Oades, 1982). In Figs. 4 and 5 the micro-scale arrangement of plant-derived OM ($^{12}C^{14}N^-$), clay minerals ($^{27}Al^{16}O^-$) and iron oxides ($^{56}Fe^{16}O^-$) is shown in close vicinity at the interface between the intact plant structure and the surrounding mineral sphere. Both fresh (Fig. 4) and more altered plant structures (collapsed cells, Fig. 5) show comparable interfaces with fine grained mineral particles. The thin layers of clay minerals and Fe oxides at these plant surfaces represent soil structures normally recovered as micro-aggregates using physical soil fractionation (Vogel et al., 2014). This clearly points to micro-aggregate like structures being rather laminar zones of high microbial activity than rounded structures as usually recovered from bulk soil samples (Fig. 2 E) or via physical fractionation. The high microbial activity can be assumed to lead to an enhanced production of gluing agents (extracellular polymeric substances) at the decaying plant surfaces (Foster, 1981; Vidal et al., 2016) fostering aggregation and thus possibly also forming precursors for more stabilized SOM (Cotrufo et al., 2013). In the present study the $fPOM_{small}$ represents the mineral-associated OM previously located in close vicinity to decomposing plant structures forming such laminar micro-aggregate like spheres. The high N content and the consequently narrow C/N ratio (Table 2) clearly demonstrate the high proportion of microbial derived OM in the $fPOM_{small}$ fraction. The micro-aggregates of the $fPOM_{small}$ itself are mostly fine grained minerals recovered by the rinsing of the larger fPOM particles, being no particulate OM in the classical meaning. Although under current conditions aggregated soil structures may be of minor importance for the overall OC stabilization when located in the permafrost layer, this will change dramatically with ongoing warming and the reported deepening of the active layer (Osterkamp and Romanovsky, 1999). A large amount of rather labile SOM is stored in the form of mostly free particulate OM (e.g. Table 2) in buried pockets transported down in deeper soil layers by cryoturbation (Gillespie et al., 2014; Mueller et al., 2015; Palmtag et al., 2016) like in the studied soil horizon (indicative for buried O horizon material). The complex aggregate structures integrating plant residues and mineral material found in the present study (e.g. Fig. 2B to E) lead to the assumption that fPOM might act as hot spots for soil aggregate formation in a warming future. Besides a presumably large amount of lost SOC due to enhanced mineralization of the mostly unaltered fPOM in warming Tundra ecosystems (Knoblauch et al., 2013; Schädel et al., 2014), part of the fPOM might act as nuclei for SOC stabilization in aggregated soil structures. This may lead to an increased proportion of occluded particulate OM in aggregated soil structures, as already indicated by the recovered oPOM (Table 2) and the structures analysed here (Fig. 2E).

Besides aggregation as a more important SOC stabilization factor in the future, the same is true for the OM directly bound to mineral surfaces recovered as mineral associated organic matter in the heavy soil fractions (sand, silt and clay). This is known as a main mechanism sequestering OC on the long term in temperate soils (Kögel-Knabner et al., 2008). In Figs. 4D and 5E the interface at the surface of a quartz grain is demonstrated by the displayed secondary ions of $^{12}C^{14}N^-$, $^{27}Al^{16}O^-$ and $^{56}Fe^{16}O^-$. The surface of the quartz grain is covered with iron oxides with associated OM and attached clay minerals indicated by the layer of $^{27}Al^{16}O^-$. It becomes clear that this FeO layer acts as a binding surface for both OM and clay minerals, thus also acting as a nucleus for soil structure formation. The vanishing of this Fe oxide layer from quartz surfaces is well known as podsolization (Lundström et al., 2000), leading to the single grain sandy texture of Podzols.

Additionally to the organo-mineral associations, there also exist clear spatial correlations between Fe and S as demonstrated in Fig. 6.

Table 3
Maximum likelihood Classification results for the soil cross section as recorded with a reflectance light microscope (RLM). Results are given as relative areas for each individual class (class) and as sums for organic and mineral classes (sum).

Class	Area [%]		Area [mm^2]	
	Class	Sum	Class	Sum
Fresh plant residues	1.9	43.1	9.6	217.8
Decomposed plant residues	17.6		89.1	
Highly decomposed OM	23.5		119.0	
Fe oxides	0.9	56.9	4.6	288.2
Coarse mineral particles	17.5		88.6	
Fine mineral fraction particles	38.5		195.0	

The ratio maps (HSI images, Fig. 6C and D) of $^{56}Fe^{16}O^-/^{32}S^-$ indicated the presence of presumably pyrite like domains in the layered iron oxide spheres. These found structures possibly link to the lacustrine phase before thaw lake drainage with distinct different redox conditions, demonstrating the unique setting of permafrost soils being an important archive for biogeochemical processes in the past.

The importance of Fe oxides for the sequestration of SOM in permafrost affected soils is clearly demonstrated by the correlating increased counts in both $^{56}Fe^{16}O^-$ and $^{12}C^{14}N^-$ at 41.8 μm shown in Fig. 4D. Nevertheless, in Fig. 4C a single strong Fe peak (at 16 μm) is not correlated with a higher CN peak, indicating that not all Fe oxides show a higher association with OM. There are numerous other small aggregated Fe oxides found throughout the measurement which show no distinctive enrichment in CN and thus SOM. This indicates that the surfaces of pedogenic iron oxides, although very important for the sequestration of OC, seem to be not completely associated with OC. This indicates a possible higher importance of aggregated soil structures (micro aggregates) for OM preservation. Thus at the same spot thicker layers of clay minerals ($^{27}Al^{16}O^-$) are located in the vicinity of the plant structure, indicating the early stages in the formation of micro-aggregates, presumably recoverable by density fractionation as $fPOM_{small}$ (Table 2). Especially the structure at 18 to 19 μm of the lateral scan (Fig. 4C) shows OM associated with clay minerals indicating a zone assignable to micro aggregate structures rich in biogeochemical interfaces. These soil structures with a high abundance of mineral associated OC in fine textured soil compartments reside in a coarse grained matrix, and are prone to relocation by freeze-thaw phenomena (cryoturbation). The development of granular, platy and lenticular soil structures due to forces originating from periodic freeze-thaw cycles including formation of segregated ice are well known for permafrost affected soils (Bockheim and Hinkel, 2012; Ping et al., 2008; Smith et al., 1991; Todisco and Bhiry, 2008). The resulting physical forces foster the mixing of mineral particles and plant residues, leading to the new formation of biogeochemical interfaces. With respect to our knowledge about the stability of organo-mineral associations in temperate soils it could be assumed that the found soil micro structures, namely soil aggregates rich in SOM, might play a crucial role in the future with ongoing global warming and thus the deepening of the active layers throughout the permafrost affected soils of the Northern hemisphere (Gentsch et al., 2015; Gillespie et al., 2014; Mueller et al., 2015).

5. Conclusions

Soil structure is an important driver for a multitude of soil functions with processes at the micro scale. One globally very important soil function in permafrost affected soils of the Northern higher latitudes is the long term storage of organic carbon. Still very little is known which mechanisms besides climatic stabilization (restricted SOM decomposition due to low temperatures) may stabilize the organic carbon when the active layers deepen in a warming future. We were able to show the tight interlinkage between soil micro structures, well known for temperate soils, and organic matter storage in a permafrost soil. Mineral associated OC from these hot spots of microbial activity were recovered from plant residues (free particulate organic matter, fPOM) as fine grained mineral fraction with a typically low C/N ratio. It is demonstrated how plant residues act as initial nucleus for the formation of micro aggregate structures composed of mineral associated OM. The biogeochemical interfaces at plant surfaces, thus act as hot spots for the formation of more complex soil structures in permafrost soils. In addition to the large number of studies on organic carbon storage and trace gas emissions in the Arctic, this study demonstrates an approach to focus on the spatial scale relevant for carbon stabilization. This work illustrates the useful combination of classical bulk analysis and state of the art spectromicroscopic techniques interlinked by computational image analysis.

Acknowledgements

We thank Christine Mlot and the Barrow Arctic Science Consortium (BASC) for assistance in field work and sampling. For assistance with the scanning electron microscope measurements we thank Marianne Hanzlik. We also thank Maria Greiner for her help with the fractionation in the laboratory at TUM, and Gabriele Matern for sample polishing at IPP in Garching. The funding for the research was provided by the NSF Postdoctoral Fellowship in Polar Regions Research (#0852036). We are also grateful to the German Science Foundation (DFG) for the financial support in the frame of the "Initiation and Intensification of International Collaboration" (MU 3021/2-1).

References

Bockheim, J.G., Hinkel, K.M., 2012. Accumulation of excess ground ice in an age sequence of drained thermokarst lake basins, Arctic Alaska. Permafr. Periglac. Process. 23 (3), 231–236.
Bullock, P., Murphy, C.P., 1980. Towards the quantification of soil structure. J. Microsc. (Oxford) 120 (DEC), 317–328.
Cotrufo, M.F., Wallenstein, M.D., Boot, C.M., Denef, K., Paul, E., 2013. The Microbial Efficiency-Matrix Stabilization (MEMS) framework integrates plant litter decomposition with soil organic matter stabilization: do labile plant inputs form stable soil organic matter? Glob. Chang. Biol. 19 (4), 988–995.
Dormaar, J.F., Foster, R.C., 1991. Nascent aggregates in the rhizosphere of perennial ryegrass (*Lolium perenne* L.). Can. J. Soil Sci. 71 (4), 465–474.
Eickhorst, T., Tippkoetter, R., 2008. Detection of microorganisms in undisturbed soil by combining fluorescence in situ hybridization (FISH) and micropedological methods. Soil Biol. Biochem. 40 (6), 1284–1293.
Fisk, A.C., Murphy, S.L., Tate, R.L., 1999. Microscopic observations of bacterial sorption in soil cores. Biol. Fertil. Soils 28 (2), 111–116.
Foster, R.C., 1981. Polysaccharides in soil fabrics. Science 214 (4521), 665–667.
Gentsch, N., Mikutta, R., Shibistova, O., Wild, B., Schnecker, J., Richter, A., Urich, T., Gittel, A., Šantrůčková, H., Bárta, J., Lashchinskiy, N., Mueller, C.W., Fuß, R., Guggenberger, G., 2015. Properties and bioavailability of particulate and mineral-associated organic matter in Arctic permafrost soils, Lower Kolyma Region, Russia. Eur. J. Soil Sci. 66, 722–734.
Gillespie, A.W., Sanei, H., Diochon, A., Ellert, B.H., Regier, T.Z., Chevrier, D., Dynes, J.J., Tarnocai, C., Gregorich, E.G., 2014. Perennially and annually frozen soil carbon differ in their susceptibility to decomposition: analysis of Subarctic earth hummocks by bioassay, XANES and pyrolysis. Soil Biol. Biochem. 68, 106–116.
Hatton, P.-J., Remusat, L., Zeller, B., Brewer, E.A., Derrien, D., 2015. NanoSIMS investigation of glycine-derived C and N retention with soil organo-mineral associations. Biogeochemistry 125 (3), 303–313.
Hinkel, K.M., Eisner, W.R., Bockheim, J.G., Nelson, F.E., Peterson, K.M., Dai, X.Y., 2003. Spatial extent, age, and carbon stocks in drained thaw lake basins on the Barrow Peninsula, Alaska. Arct. Antarct. Alp. Res. 35 (3), 291–300.
Höfle, S., Rethemeyer, J., Mueller, C.W., John, S., 2013. Organic matter composition and stabilization in a polygonal tundra soil of the Lena-Delta. Biogeosciences 10, 3145–3158.
Hugelius, G., Strauss, J., Zubrzycki, S., Harden, J.W., Schuur, E.A.G., Ping, C.L., Schirrmeister, L., Grosse, G., Michaelson, G.J., Koven, C.D., O'Donnell, J.A., Elberling, B., Mishra, U., Camill, P., Yu, Z., Palmtag, J., Kuhry, P., 2014. Estimated stocks of circumpolar permafrost carbon with quantified uncertainty ranges and identified data gaps. Biogeosciences 11 (23), 6573–6593.
Knoblauch, C., Beer, C., Sosnin, A., Wagner, D., Pfeiffer, E.M., 2013. Predicting long-term carbon mineralization and trace gas production from thawing permafrost of Northeast Siberia. Glob. Chang. Biol. 19 (4), 1160–1172.
Kögel-Knabner, I., Guggenberger, G., Kleber, M., Kandeler, E., Kalbitz, K., Scheu, S., Eusterhues, K., Leinweber, P., 2008. Organo-mineral associations in temperate soils: integrating biology, mineralogy, and organic matter chemistry. J. Plant Nutr. Soil Sci. 171, 61–82.
Kubiena, W.L., 1938. Micropedology. Micropedology. Collegiate Press, Ames, Iowa.
Li, Y., Dick, W.A., Tuovinen, O.H., 2004. Fluorescence microscopy for visualization of soil microorganisms - a review. Biol. Fertil. Soils 39 (5), 301–311.
Lundström, U.S., van Breemen, N., Bain, D., 2000. The podzolization process. A review. Geoderma 94 (2–4), 91–107.
Martens, D.A., 2000. Plant residue biochemistry regulates soil carbon cycling and carbon sequestration. Soil Biol. Biochem. 32 (3), 361–369.
Mueller, C.W., Weber, P.K., Kilburn, M.R., Hoeschen, C., Kleber, M., Pett-Ridge, J., 2013. Advances in the analysis of biogeochemical interfaces: NanoSIMS to investigate soil microenvironments. Adv. Agron. 121 (121), 1–46.
Mueller, C.W., Rethemeyer, J., Kao-Kniffin, J., Löppmann, S., Hinkel, K.M., Bockheim, J.G., 2015. Large amounts of labile organic carbon in permafrost soils of northern Alaska. Glob. Chang. Biol. 21 (7) m.
Murton, J.B., Goslar, T., Edwards, M.E., Bateman, M.D., Danilov, P.P., Savvinov, G.N., Gubin, S.V., Ghaleb, B., Haile, J., Kanevskiy, M., Lozhkin, A.V., Lupachev, A.V., Murton, D.K., Shur, Y., Tikhonov, A., Vasil'chuk, A.C., Vasil'chuk, Y.K., Wolfe, S.A., 2015. Palaeoenvironmental interpretation of yedoma silt (ice complex) deposition as cold-climate loess, Duvanny Yar, Northeast Siberia. Permafr. Periglac. Process. 26 (3), 208–288.

Oades, J.M., Waters, A.G., 1991. Aggregate hierarchy in soils. Aust. J. Soil Res. 29 (6), 815–828.
Osterkamp, T.E., Romanovsky, V.E., 1999. Evidence for warming and thawing of discontinuous permafrost in Alaska. Permafr. Periglac. Process. 10 (1), 17–37.
Palmtag, J., Ramage, J., Hugelius, G., Gentsch, N., Lashchinskiy, N., Richter, A., Kuhry, P., 2016. Controls on the storage of organic carbon in permafrost soil in northern Siberia. Eur. J. Soil Sci. 67 (4), 478–491.
Ping, C.L., Michaelson, G.J., Kimble, J.M., Romanovsky, V.E., Shur, Y.L., Swanson, D.K., Walker, D.A., 2008. Cryogenesis and soil formation along a bioclimate gradient in Arctic North America. J. Geophys. Res. Biogeosci. 113 (G3).
Pulleman, M.M., Six, J., van Breemen, N., Jongmans, A.G., 2005. Soil organic matter distribution and microaggregate characteristics as affected by agricultural management and earthworm activity. Eur. J. Soil Sci. 56 (4), 453–467.
Richards, J.A., Jia, X., 1999. Remote Sensing Digital Image Analysis. third ed. Springer, Berlin, Heidelberg, New York.
Schädel, C., Schuur, E.A.G., Bracho, R., Elberling, B., Knoblauch, C., Lee, H., Luo, Y.Q., Shaver, G.R., Turetsky, M.R., 2014. Circumpolar assessment of permafrost C quality and its vulnerability over time using long-term incubation data. Glob. Chang. Biol. 20 (2), 641–652.
Schuur, E.A.G., Bockheim, J., Canadell, J.G., Euskirchen, E., Field, C.B., Goryachkin, S.V., Hagemann, S., Kuhry, P., Lafleur, P.M., Lee, H., Mazhitova, G., Nelson, F.E., Rinke, A., Romanovsky, V.E., Shiklomanov, N., Tarnocai, C., Venevsky, S., Vogel, J.G., Zimov, S.A., 2008. Vulnerability of permafrost carbon to climate change: implications for the global carbon cycle. Bioscience 58 (8), 701–714.
Smith, C.A.S., Fox, C.A., Hargrave, A.E., 1991. Development of soil structure in some turbic cryosols in the Canadian low arctic. Can. J. Soil Sci. 71 (1), 11–29.
Staff, Soil Survey, 2010. Keys to Soil Taxonomy. USDA Natural Resources Conservation Service, Washington D.C.
Szymanski, W., Skiba, M., Wojtun, B., Drewnik, M., 2015. Soil properties, micromorphology, and mineralogy of Cryosols from sorted and unsorted patterned grounds in the Hornsund area, SW Spitsbergen. Geoderma 253, 1–11.
Tisdall, J.M., Oades, J.M., 1982. Organic matter and water-stable aggregates in soils. J. Soil Sci. 33 (2), 141–163.
Todisco, D., Bhiry, N., 2008. Micromorphology of periglacial sediments from the Tayara site, Qikirtaq Island, Nunavik (Canada). Catena 76 (1), 1–21.
Totsche, K.U., Rennert, T., Gerzabek, M.H., Koegel-Knabner, I., Smalla, K., Spiteller, M., Vogel, H.-J., 2010. Biogeochemical interfaces in soil: the interdisciplinary challenge for soil science. J. Plant Nutr. Soil Sci. 173 (1), 88–99.
Trumbore, S., 2009. Radiocarbon and soil carbon dynamics. Annu. Rev. Earth Planet. Sci. 37, 47–66.
Vidal, A., Remusat, L., Watteau, F., Derenne, S., Quenea, K., 2016. Incorporation of 13C labelled shoot residues in *Lumbricus terrestris* casts: a combination of transmission electron microscopy and nanoscale secondary ion mass spectrometry. Soil Biol. Biochem. 93, 8–16.
Vogel, C., Mueller, C.W., Hoeschen, C., Buegger, F., Heister, K., Schulz, S., Schloter, M., Koegel-Knabner, I., 2014. Submicron structures provide preferential spots for carbon and nitrogen sequestration in soils. Nat. Commun. 5.
von Lützow, M., Kögel-Knabner, I., Ludwig, B., Matzner, E., Flessa, H., Ekschmitt, K., Guggenberger, G., Marschner, B., Kalbitz, K., 2008. Stabilization mechanisms of organic matter in four temperate soils: development and application of a conceptual model. J. Plant Nutr. Soil Sci. 171, 111–124.
Vonk, J.E., Gustafsson, O., 2013. Permafrost-carbon complexities. Nat. Geosci. 6 (9), 675–676.